Supplementary Information

Solution-Processed Yolk-Shell-Shaped $WO_3/BiVO_4$ Heterojunction Photoelectrode for Efficient Solar Water Splitting

Bingjun Jin,‡[a] Eunji Jung,‡[b] Ming Ma,[c] Sung Soon Kim,[a] Kan Zhang,[ad] Jin Il Kim,[a] Yongkeun Son*[b] and Jong Hyeok Park*[a]

[a] Department of Chemical and Biomolecular Engineering, Yonsei University, 50 Yonsei-ro, Seodaemun-gu, Seoul 120-749, Republic of Korea

[b] Department of Chemistry, BK21plus School of HRD Center for Creative Convergence Chemical Science, Sungkyunkwan University, Suwon 440-746, Republic of Korea

[c] SKKU Advanced Institute of Nano Technology Sungkyunkwan University, Suwon 440-746, Republic of Korea

[d] MIIT Key Laboratory of Advanced Display Materials and Devices, Institute of Optoelectronics and Nanomaterials, College of Materials Science and Engineering, Nanjing University of Science and Technology, Nanjing 210094, P. R. China

‡These authors contributed equally to this work.

*Corresponding Author: Email: ykson@skku.edu (Y. Son) and lutts@yonsei.ac.kr (J. H. Park)

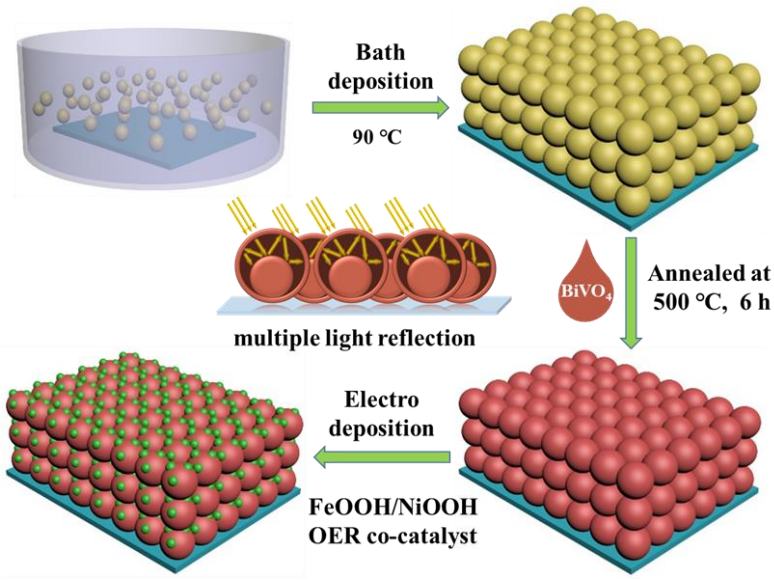

Scheme S1 Schematic diagram of the fabrication process for the WO_3/$BiVO_4$/OER photoanodes and multiple light reflection of yolk-shell structure WO_3.

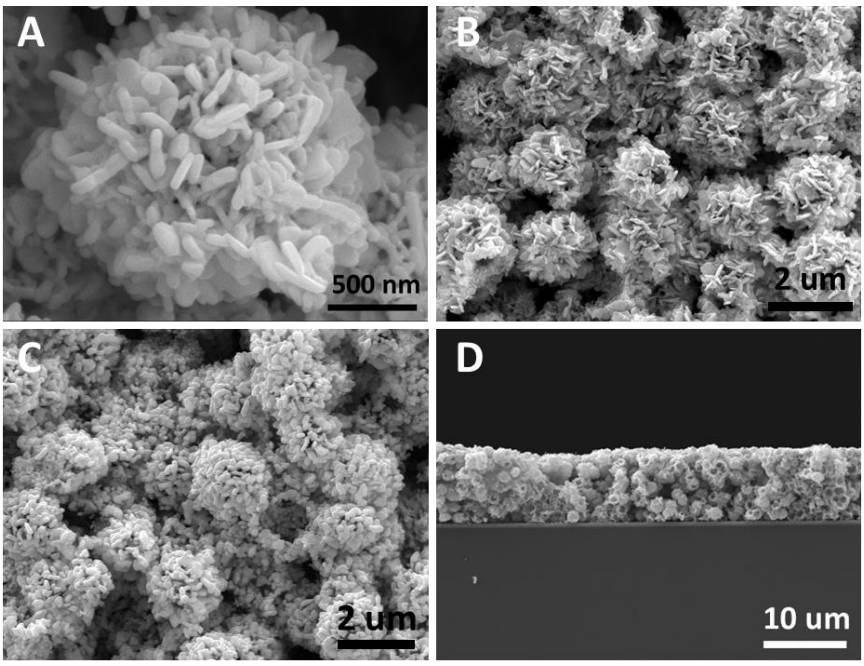

Fig. S1 Top-view images of (A, B) yolk-shell $WO_3/BiVO_4$ heterojunction with 80 µl of $BiVO_4$ and (C) modified with OER co-catalyst; (D) Cross-sectional images of the yolk-shell $WO_3/BiVO_4$ heterojunction.

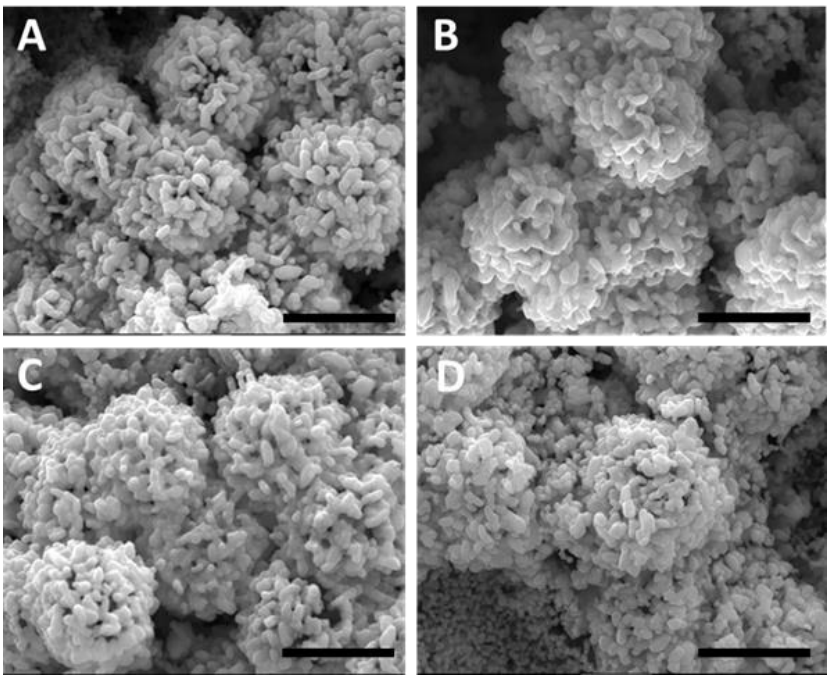

Fig. S2 Top-view SEM images of Y-WO_3/$BiVO_4$ with different amounts of $BiVO_4$: (A) 40 µl, (B) 60 µl, (C) 80 µl, and (D) 100 µl (scale bars are 2 um).

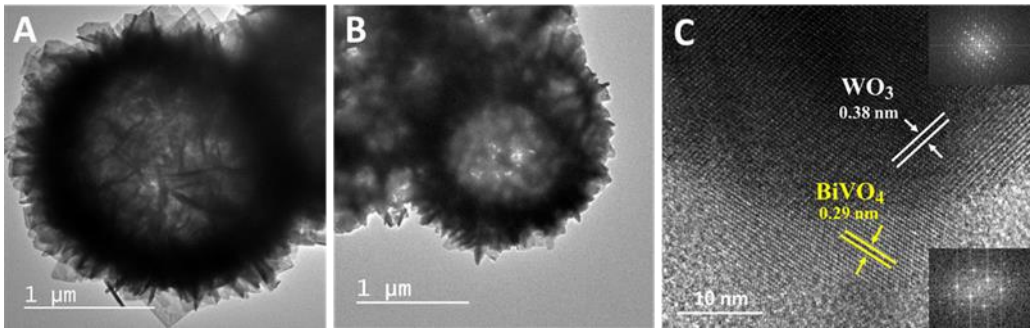

Fig. S3 TEM images of (A) WO_3 nanosphere; (B) WO_3/$BiVO_4$ heterojunction after coating with $BiVO_4$ layer; and (C) HR-TEM images of WO_3/$BiVO_4$ heterojunction, the insets are the corresponding selected-area electron diffraction patterns.

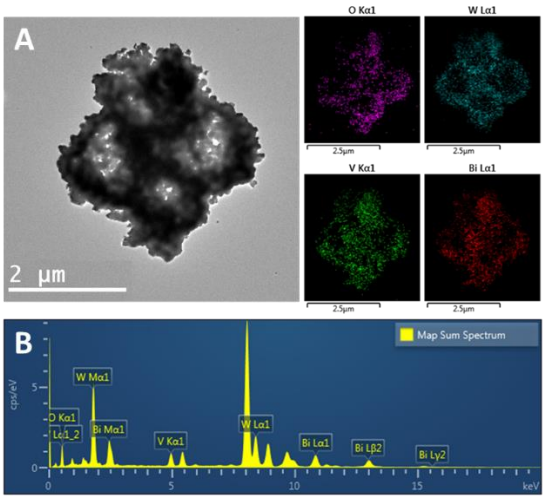

Fig. S4 (A) TEM images of $WO_3/BiVO_4$ heterojunction and the corresponding surface elements distribution; (B) EDX of $WO_3/BiVO_4$ heterojunction.

It can be seen from Fig. S3 that after coating with $BiVO_4$ to form $WO_3/BiVO_4$ heterojunction (B), the heterojunction still remain the original structure relatively which was also displayed by the SEM image at Fig.1C in the manuscript. The $BiVO_4$ layer and the corresponding elements of the uniform dispersion of the Bi and V elements are also be showed in Fig. S4, which suggesting the $BiVO_4$ was uniformly combined with WO_3. The lattice spacing of 0.38 nm in Fig. S3C is well matched with the (002) crystalline plane of monoclinic WO_3 and the measured lattice spacing of 0.29 nm corresponds the (040) plane of monoclinic $BiVO_4$, while the selected area electron diffraction patterns indicate that the crystal lattice fringes observed originate from (002) WO_3 and (040) $BiVO_4$. On the other hand, the SAED pattern indicates the single-crystal feature with the typical crystal zone axis of [001]. Overall, it indicates that the $BiVO_4$ layer can cover the entire surface of the WO_3 nanospheres through our method, the well-defined interface is also important for charge separation in the heterojunction.

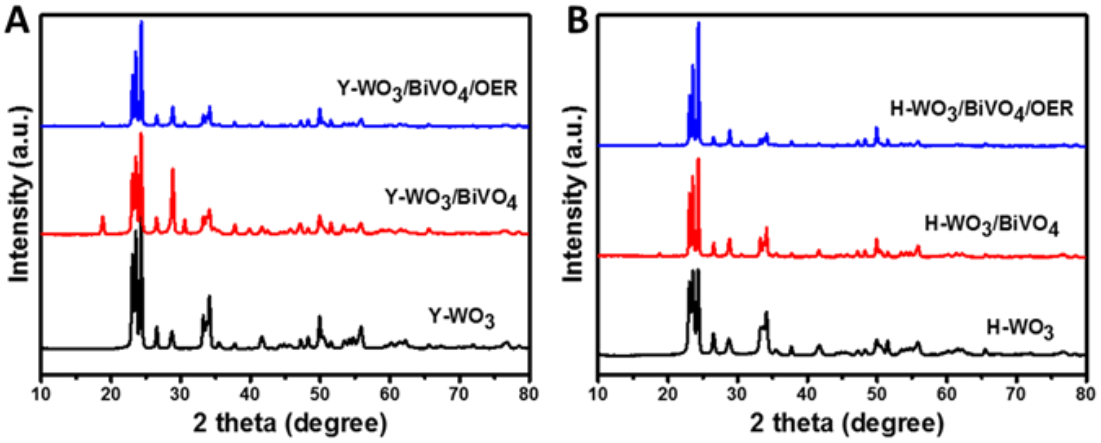

Fig. S5 XRD patterns of (A): the yolk-shell WO_3, Y-WO_3/$BiVO_4$ and Y-WO_3/$BiVO_4$/OER samples; (B): the hollow WO_3, H-WO_3/$BiVO_4$ and H-WO_3/$BiVO_4$/OER samples.

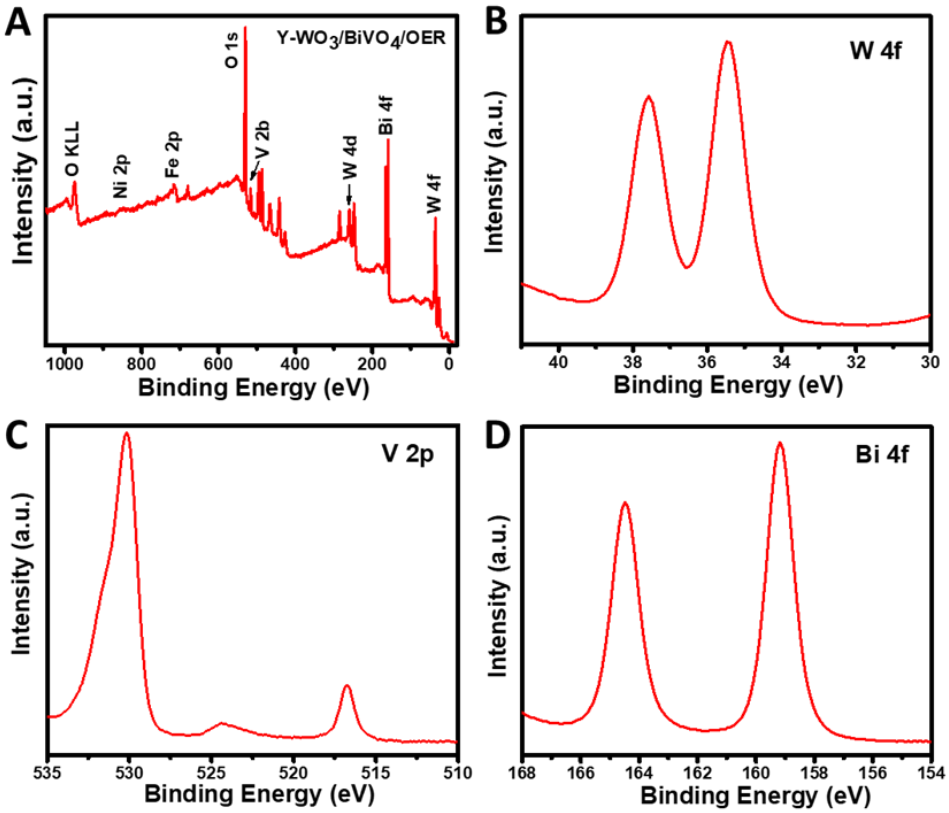

Fig. S6 (A) XPS spectra of a survey scan of Y-WO_3/$BiVO_4$/OER and the corresponding XPS elemental spectra of (B) W 4f, (C) V 2p, and (D) Bi 4f.

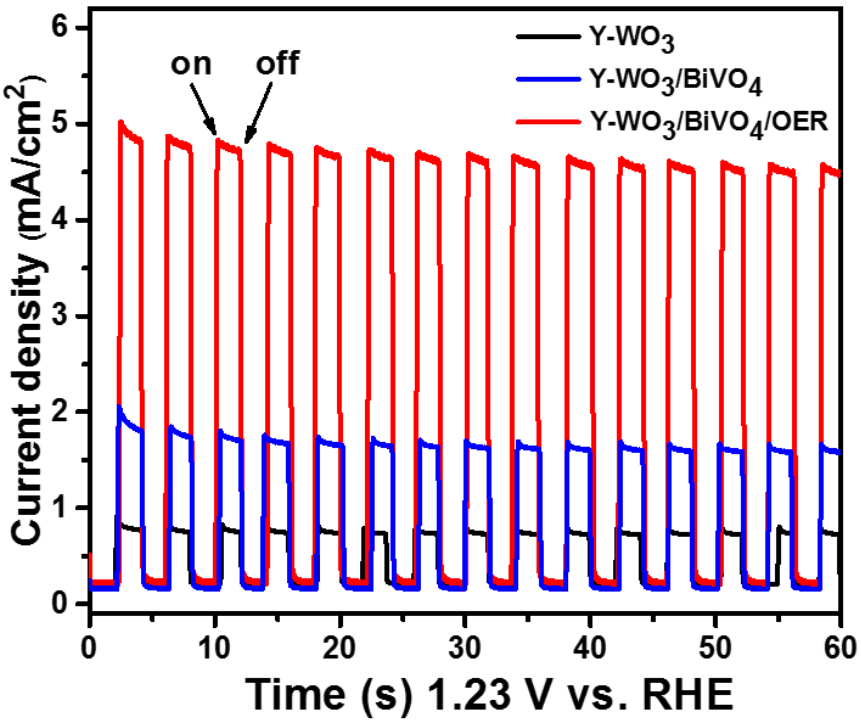

Fig. S7 Photocurrent-time (I–t) curves of the samples (the amount of $BiVO_4$ precursor is 80 μl) in a 0.5 M Na_2SO_4 solution under AM 1.5G light illumination at 1.23 V (vs. RHE).

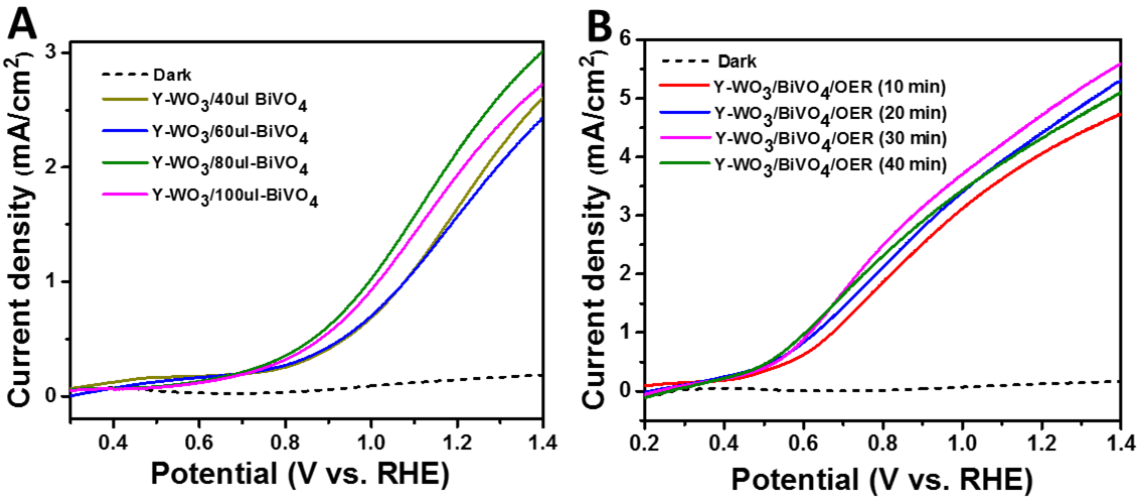

Fig. S8 LSV scans of Y-WO_3/$BiVO_4$ (A) with various amount of $BiVO_4$ precursor and (B) with different electrodeposition times of the OER co-catalyst layer.

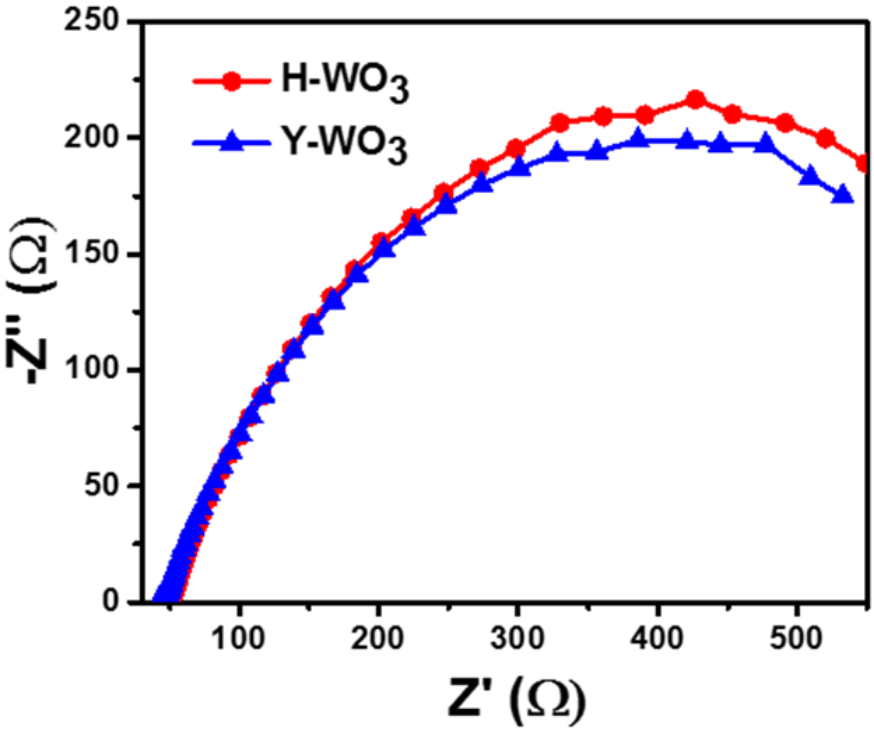

Fig. S9 Nyquist plots of the hollow WO_3 and yolk-shell WO_3 photoanodes at 1.23 V (vs. RHE).

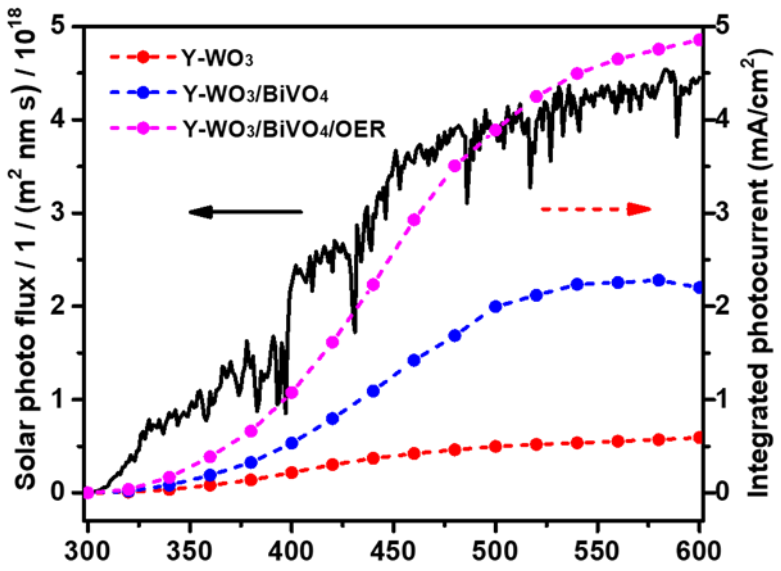

Fig. S10 Integrated photocurrent over the standard solar spectrum dependence on the IPCE on wavelength for the photoanodes at 1.23 V vs. RHE.

Discussion:

The photocurrent ($I(\lambda)$) was predicted by convolution of the IPCE spectra with the photo flux density distribution as the following equation,

$$I(\lambda) = \int qF(\lambda)\, IPCE(\lambda) d\lambda$$

where q is the electron charge and F(λ) is the incident photon flux density (AM 1.5, ASTM G173) at wavelength λ, IPCE(λ) data is shown in Fig. 3D in the manuscript.

References:

1 S. D. Tilley, M. Cornuz, K. Sivula and M. Grätzel, Angew. Chem. Int. Ed., 2010, **122**, 6549-6552.

2 C.-J. Lin, W.-Y. Yu and S.-H. Chien, J. Mater. Chem., 2010, **20**, 1073-1077.

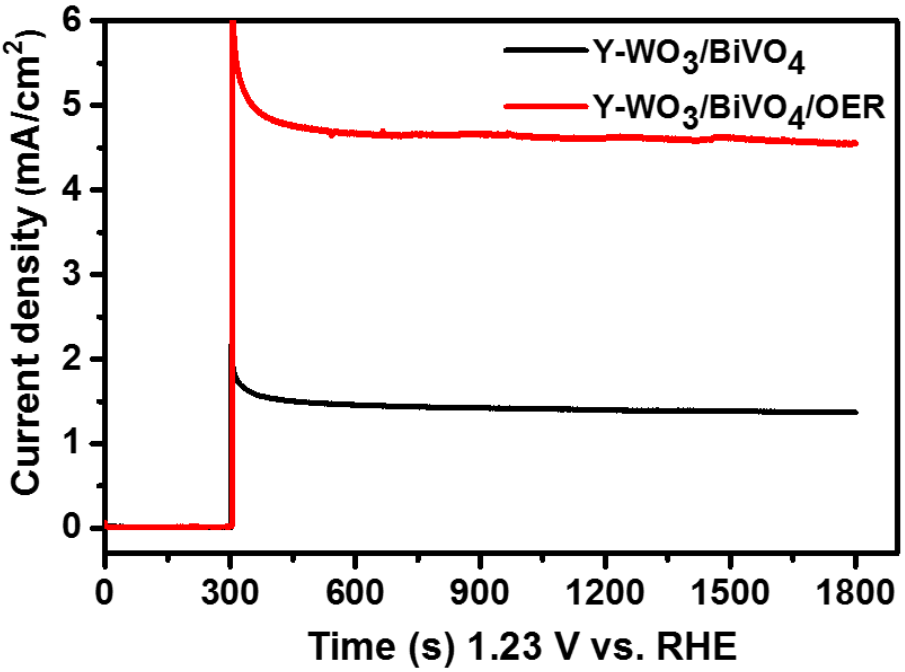

Fig. S11 Photocurrent stability of the Y-WO_3/$BiVO_4$ and Y-WO_3/$BiVO_4$/OER photoanode at 1.23 V vs. RHE.

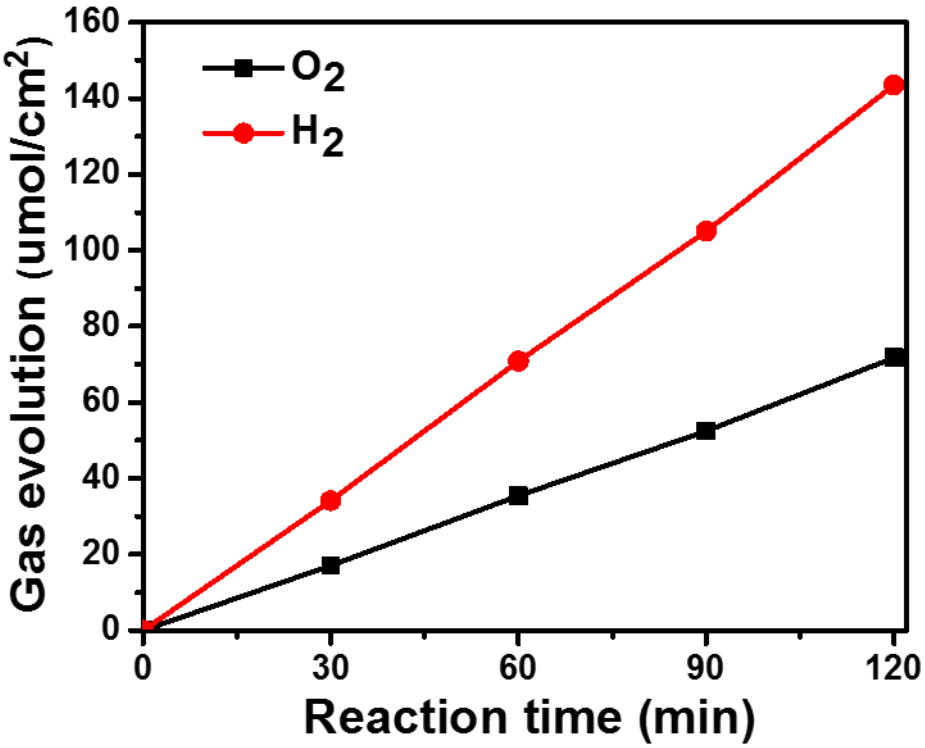

Fig. S12 H_2 and O_2 evolution at 1.2 V versus the Pt counter electrode of the Y-WO_3/$BiVO_4$/OER photoanode.

The faradaic efficiency for O_2 evolution is determined by the following equation:

$$\eta_{Faradaic} = \frac{4 \times N_{O_2}(mol) \times 96485(Cmol^{-1})}{Q(C)}$$

where η_{Faradaic} is the faradaic efficiency for photoelectrochemical water oxidation, N_{O_2} is the amount of oxygen, and Q is the total amount of generated charge (Q = photocurrent × time). Therefore, the faradaic efficiency for O_2 evolution is calculated to be 87.7%. The loss of faradaic efficiency was possibly due to the limited kinetics of water oxidation and back reaction of H_2 and O_2.

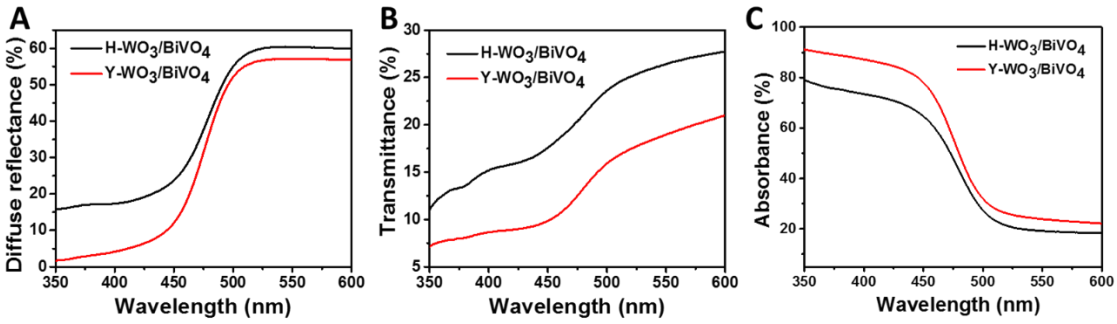

Fig. S13 (A) Diffuse reflectance curves, (B) transmittance spectra and (C) UV−vis absorption spectra of hollow $WO_3/BiVO_4$ and yolk-shell $WO_3/BiVO_4$.

References:

S1 M. G. Mali, H. Yoon, M. Kim, M. T. Swihart, S. S. Al-Deyab and S. S. Yoon, Appl. Phys. Lett., 2015, **106**, 151603.

S2 J. Su, L. Guo, N. Bao and C. A. Grimes, Nano Lett., 2011, **11**, 1928-1933.

S3 P. M. Rao, L. Cai, C. Liu, I. S. Cho, C. H. Lee, J. M. Weisse, P. Yang and X. Zheng, Nano Lett., 2014, **14**, 1099-1105.

S4 H. Zhang, W. Zhou, Y. Yang and C. Cheng, small, 2017, **13**, 1603840.

S5 Y. Pihosh, I. Turkevych, K. Mawatari, T. Asai, T. Hisatomi, J. Uemura, M. Tosa, K. Shimamura, J. Kubota, K. Domen and T. Kitamori, small, 2014, **10,** 3692-3699.

S6 Y. Pihosh, I. Turkevych, K. Mawatari, J. Uemura, Y. Kazoe, S. Kosar, K. Makita, T. Sugaya, T. Matsui, D. Fujita, M. Tosa, M. Kondo and T. Kitamori, Sci. Rep., 2015, **5**, 11141.

S7 J. H. Baek, B. J. Kim, G. S. Han, S. W. Hwang, D. R. Kim, I. S. Cho and H. S. Jung, ACS Appl. Mater. Interfaces, 2017, **9**, 1479-1487.

S8 S. S. Kalanur, I.-H. Yoo, J. Park and H. Seo, J. Mater. Chem. A, 2017, **5**, 1455-1461.

S9 S. Y. Chae, H. Jung, H. S. Jeon, B. K. Min, Y. J. Hwang and O.-S. Joo, J. Mater. Chem. A, 2014, **2**, 11408-11416.

S10 S. Y. Chae, C. S. Lee, H. Jung, O.-S. Joo, B. K. Min, J. H. Kim and Y. J. Hwang, ACS Appl. Mater. Interfaces, 2017, **9**, 19780-19790.

S11 I. Grigioni, K. G. Stamplecoskie, E. Selli and P. V. Kamat, J. Phys. Chem. C, 2015, **119**, 20792-20800.